

# The Megamaser Cosmology Project: I. VLBI observations of UGC 3789

M. J. Reid<sup>1</sup>, J. A. Braatz<sup>2</sup>, J. J. Condon<sup>2</sup>, L. J. Greenhill<sup>1</sup>, C. Henkel<sup>3</sup>, K. Y. Lo<sup>2</sup>

## ABSTRACT

The Megamaser Cosmology Project (MCP) seeks to measure the Hubble Constant ( $H_0$ ) in order to improve the extragalactic distance scale and constrain the nature of dark energy. We are searching for sources of  $H_2O$  maser emission from AGN with sub-pc accretion disks, as in NGC 4258, and following up these discoveries with Very Long Baseline Interferometric (VLBI) imaging and spectral monitoring. Here we present a VLBI map of the  $H_2O$  masers toward UGC 3789, a galaxy well into the Hubble Flow. We have observed masers moving at rotational speeds up to  $800 \text{ km s}^{-1}$  at radii as small as  $0.08 \text{ pc}$ . Our map reveals masers in a nearly edge-on disk in Keplerian rotation about a  $10^7 M_\odot$  supermassive black hole. When combined with centripetal accelerations, obtained by observing spectral drifts of maser features (to be presented in Paper II), the UGC 3789 masers may provide an accurate determination of  $H_0$ , independent of luminosities and metallicity and extinction corrections.

Subject headings: Hubble Constant | Cosmology | Dark Energy | General Relativity | distances | individual sources (UGC 3789)

## 1. Introduction

The current "concordance" cosmological model assumes a flat  $\Lambda$ CDM universe composed of baryons, cold dark matter, and "dark energy" that accelerates the expansion of the universe (Spergel et al. 2003). The location of the first peak in the angular power spectrum

---

<sup>1</sup>Harvard-Smithsonian Center for Astrophysics, 60 Garden Street, Cambridge, MA 02138, USA

<sup>2</sup>National Radio Astronomy Observatory, 520 Edgemont Road, Charlottesville, VA 22903

<sup>3</sup>Max-Planck-Institut für Radioastronomie, Auf dem Hügel 69, 53121 Bonn, Germany

of the cosmic microwave background (CMB) radiation determines the angular-size distance to the surface of last scattering. This distance depends on the amount of dark energy and the geometry and current expansion rate of the universe,  $H_0$ . If one does not assume that the universe is flat, the CMB data alone are consistent with a wide range of values of  $H_0$ . Thus, independent measurements of  $H_0$  are needed to justify the flatness assumption and to determine whether dark energy is the cosmological constant,  $\Lambda$ , of General Relativity, a variable "quintessence" (Wetterich 1988; Ratra & Peebles 1988), or possibly something else. Hu (2005) concludes that the most important single complement to CMB data would be a precise (e.g. 1% uncertainty) measurement of  $H_0$ .

The current "best value" for the Hubble Constant,  $H_0 = 72 \pm 7 \text{ km s}^{-1} \text{ Mpc}^{-1}$  from the HST Key Project (Freedman et al. 2001), is based on luminosity distance measurements to extragalactic Cepheid variables treated as "standard candles." The 10% uncertainty in  $H_0$  is dominated by systematic errors that cannot easily be reduced by observations of more galaxies.

Very Long Baseline Array (VLBA) observations of the  $\text{H}_2\text{O}$  megamaser in the nearby Seyfert 2 galaxy NGC 4258 have provided an accurate, angular-diameter distance to the galaxy (Hernstein et al. 1999), bypassing the problems of standard candles. The  $\text{H}_2\text{O}$  masers in NGC 4258 arise in a thin (annular) disk viewed nearly edge-on (Greenhill et al. 1995a) and appear at galactocentric radii  $R = 0.14$  to  $0.28 \text{ pc}$ . Maser lines near the systemic velocity of the galaxy come from gas moving across the sky on the near side of the disk, and "high-velocity lines," with relative velocities of up to  $V = 1100 \text{ km s}^{-1}$ , come from gas moving along the line of sight at the disk tangent points. The high-velocity lines display a Keplerian rotation curve, implying a central mass of  $4 \times 10^7 M_\odot$ , presumably in the form of a supermassive black hole (SMBH) (Miyoshi et al. 1995).

For NGC 4258, the velocities of individual systemic features are observed to increase by  $9 \text{ km s}^{-1} \text{ yr}^{-1}$  (Haschick, Baan & Peng 1994; Greenhill et al. 1995b), allowing a direct measurement of the centripetal acceleration ( $a = V^2/R$ ) of clouds moving across our line of sight near the nucleus (Watson & Wallin 1994). Conceptually, the angular-diameter distance,  $D$ , to NGC 4258 can be determined geometrically by dividing the linear radius of masers, measured from Doppler shifts and accelerations ( $R = V^2/a$ ), by their angular radius, measured from a Very Long Baseline Interferometric (VLBI) image ( $\theta_R$ ). Maser proper motions can also be used to measure distance, but generally yield less accurate distances than using accelerations. Observations with the VLBA of the  $\text{H}_2\text{O}$  masers in NGC 4258 have been carefully modeled, yielding the most accurate distance ( $D = 7.2 \pm 0.5 \text{ Mpc}$ ) to date for a galaxy (Hernstein et al. 1999).

Unfortunately, NGC 4258 is too close to determine  $H_0$  directly (i.e. by dividing its recess-

sional velocity of  $475 \text{ km s}^{-1}$  by its distance), since the galaxy's deviation from the Hubble flow could be a significant fraction of its recessional velocity. Instead, the measured distance to NGC 4258 has been used to anchor the zero point of the Cepheid period-luminosity relation (Newman et al. 2001; Macri et al. 2006; Argon et al. 2007; Humphreys et al. 2008). However, galaxies with edge-on, disk-like  $\text{H}_2\text{O}$  masers, similar to those in NGC 4258, that are distant enough to be in the Hubble flow ( $D > 30 \text{ Mpc}$ ) could be used to measure  $H_0$  directly (Greenhill 2004).

Surveys of galaxies for nuclear  $\text{H}_2\text{O}$  masers have been quite successful and have identified more than 100 extragalactic nuclear  $\text{H}_2\text{O}$  masers (Claussen & Lo 1986; Braatz, Wilson & Henkel 1996; Greenhill et al. 2002; Henkel et al. 2002; Greenhill et al. 2003; Braatz et al. 2004; Kondratko et al. 2006; Kondratko, Greenhill & Moran 2006; Braatz & Gugliucci 2008). In order to coordinate efforts to find and image new sources of nuclear  $\text{H}_2\text{O}$  masers, we formed a team of scientists active in this area of research from the Harvard-Smithsonian Center for Astrophysics, the National Radio Astronomy Observatory (NRAO), and the Max-Planck-Institut für Radioastronomie (MPIfR). This effort, called the Megamaser Cosmology Project (MCP), is aimed at measuring  $H_0$  directly, with  $\sim 3\%$  accuracy, using a combination of VLBI imaging and single-dish monitoring of nuclear  $\text{H}_2\text{O}$  masers toward  $\sim 10$  galaxies.

Recently Braatz & Gugliucci (2008) discovered a relatively strong  $\text{H}_2\text{O}$  maser ( $S_{0.1 \text{ Jy}}$ ) toward the Seyfert 2 nucleus of UGC 3789. The  $\text{H}_2\text{O}$  maser spectrum has the characteristics of an edge-on disk similar to NGC 4258. The UGC 3789 masers span  $1500 \text{ km s}^{-1}$  in Doppler shift and the systemic masers were observed to accelerate by up to  $8.1 \text{ km s}^{-1} \text{ yr}^{-1}$ , suggesting an origin in a sub-pc disk about a  $10^7 M_\odot$  black hole.

In this paper, and in Braatz et al. (2008) (hereafter Paper II), we report results leading to the first MCP measurement of  $H_0$ . Sensitive VLBI observations and images of the nuclear  $\text{H}_2\text{O}$  masers toward UGC 3789 are presented in this paper. In Paper II, we present monitoring observations with large single-dish telescopes, which yield accelerations of  $\text{H}_2\text{O}$  masers. The combination of the VLBI imaging and the single-dish acceleration data may yield a measurement of  $H_0$  with an accuracy comparable to that of the Hubble Key Project.

## 2. Observations, Calibration, and Imaging

We observed UGC 3789 on 2006 December 10 for a total of 12 hours, with the 10 NRAO<sup>1</sup> VLBA antennas (under program BB227A), augmented by the Green Bank Telescope (GBT) and the Eelsberg 100-m telescope<sup>2</sup>. The coordinates of the sources observed are listed in Table 1. We alternated between two observing modes: (1) a 60-min block of continuous tracking of UGC 3789 (self-calibration mode) and (2) a 45-min block of rapid switching between UGC 3789 and a nearby compact continuum source J0728+5907 (phase-referencing mode). The phase-referencing blocks were a "back-up" in the event that the UGC 3789 maser signal was not strong enough for self-calibration. Both observing modes were successful. However, since the self-calibration mode produced a much higher on-source duty cycle and better phase calibration than the phase-referencing mode, we only report results from the total of 5 hr of self-calibration mode observations.

With a maximum recording rate of 512 Mbits s<sup>-1</sup>, we could cover the entire range of detectable UGC 3789 H<sub>2</sub>O maser emission, but not with dual-polarization for all frequency bands. We centered 16-MHz bands at LSR velocities (optical definition) as follows: left circularly polarized (LCP) bands at 3880, 3710, 3265, 2670 and 2500 km s<sup>-1</sup> and right circularly polarized (RCP) at 3880, 3265 and 2670 km s<sup>-1</sup>. The signals were sampled at the Nyquist rate (32 Mbits s<sup>-1</sup>) and with 2 bits per sample.

We placed "geodetic" blocks at the start and end of our observations, in order to solve for atmospheric and clock delay residuals for each antenna (Reid & Brunthaler 2004). In these blocks we rapidly cycled among 14 compact radio sources that spanned a wide range of zenith angles at all antennas. These data were taken in left circular polarization with eight 16-MHz bands that spanned 492 MHz of bandwidth between 22.00 and 22.49 GHz; the bands were spaced in a "minimum redundancy" manner to sample, as uniformly as possible, all frequency differences. The data were correlated, corrected for ionospheric delays using total electron content measurements (Walker & Chatterjee 2000), and residual multi-band delays and fringe rates were determined for all sources. The multi-band delays and fringe rates were modeled as owing to a vertical atmospheric delay and delay-rate, as well as a clock offset and clock drift rate, at each antenna. Using a least-squares fitting program, we estimated zenith atmospheric path-delays and clock errors with accuracies typically 0.5 cm and 0.03 nsec, respectively.

---

<sup>1</sup>The National Radio Astronomy Observatory is operated by Associated Universities, Inc., under a cooperative agreement with the National Science Foundation.

<sup>2</sup>The Eelsberg 100-m telescope is a facility of the Max-Planck-Institut für Radioastronomie

We observed the strong continuum source, J0753+ 5352, hourly in order to monitor delay and electronic phase differences among and across the IF bands. Generally, variations of phase across the VLBA bandpasses are small ( $< 5^\circ$ ) across the central 90% of the band and thus we needed no bandpass corrections. We tested the effect of bandpass corrections, using the J0753+ 5352 data, and found position differences of  $\sim 0.002$  mas from user features mid-way between the band center and band edge.

The raw data recorded at each antenna were cross-correlated with an integration time of 1.05 sec at the VLBA correlation facility in Socorro, NM. For this short integration time we had to correlate the data in two passes in order to achieve sufficient spectral resolution (128 spectral channels for each IF band) without exceeding the maximum correlator output rate. Before calibration, the two correlation data sets were "glued" together.

We calibrated the data using the NRAO Astronomical Image Processing System (AIPS). First, we corrected interferometer delays and phases for the effects of diurnal feed rotation (parallactic angle) and for small errors in the values of the Earth's orientation parameters used at the time of correlation. By analyzing the data taken in phase-referencing mode, we determined that the strong maser feature at  $V_{\text{LSR}} = 2689 \text{ km s}^{-1}$ , which we later used as the phase reference for the self-calibration mode data, was offset from the position of UGC 3789 used in the VLBA correlator by  $(1; 15)$  mas toward (east,north), respectively, relative to J0728+ 5907.

Since the VLBA correlator model includes no ionospheric delays, we used global total electron content models to remove ionospheric effects. We then corrected the data for residual zenith atmospheric delays and clock drifts, as determined from the geodetic block data. While we obtained good atmospheric/clock corrections for most antennas, insufficient data were obtained for the Eelsberg (EB) and Mauna Kea (MK) antennas for this task. Thus, we later used the data from the hourly observations of J0753+ 5352 to determine final delay corrections for the UGC 3789 data.

We corrected the interferometer visibility amplitudes for the few percent effects of biases in the threshold levels of the data samplers at each antenna. We also entered system temperature and antenna gain curve information into calibration tables. These tables were used later to convert correlation coefficients to flux densities. Next, we performed a "manual phase-calibration" to remove delay and phase differences among all bands. This was accomplished with data from one scan on a strong calibrator, 4C 39.25. We did not shift the frequency axes of the maser interferometer spectra to compensate for the Doppler shift changes during the 5 hr UGC 3789 observing track, as these effects were less than our velocity resolution of  $1.7 \text{ km s}^{-1}$ .

The final calibration involved selecting a maser feature as the interferometer phase-reference. The strongest maser feature in the spectrum peaked at 0.07 Jy and was fairly broad. We found that using 5 channels spanning an LSR velocity range of 2685 to 2692 km s<sup>-1</sup> (i.e. channels 52 to 56 from the blue-shifted high velocity band centered at  $V_{\text{LSR}} = 2670$  km s<sup>-1</sup>), adding together both polarizations, and fitting fringes over a 1 m in period gave optimum results. The St. Croix (SC) antenna failed to produce phase-reference solutions and data from that antenna were discarded. For most antennas at most times the phases could be easily interpolated between solutions. However, when the differences between adjacent reference phases exceeded 60°, the data between those times were discarded. This editing was done on baseline (not antenna) data, since correlated phases between antennas do not affect interferometer coherence.

After calibration, we Fourier transformed the gridded (u,v)-data to make images of the maser emission in all spectral channels for each of the two IF bands. The point-source response function had FWHM of 0.35 × 0.22 mas elongated along a position angle of 17° east of north. The images were deconvolved with the point-source response using the CLEAN algorithm and restored with a circular Gaussian beam with a 0.30 mas FWHM. All images appeared to contain single, point-like maser spots. We then fitted each spectral channel image with an elliptical Gaussian brightness distribution in order to obtain positions and flux densities.

### 3. Results & Discussion

Channel maps typically had rms noise levels of 0.9 mJy for the dual-polarized IF bands and 1.2 mJy for the single-polarization IF bands. The flux densities from the Gaussian fits for all spectral channels in all IF bands were used to generate the interferometer spectrum shown in Fig. 1. When little signal was detected in a spectral channel, as evidenced by a failed fit or a spot size greater than 1 mas, we assigned that channel zero flux density.

The flux densities and positions determined by Gaussian fitting each spectral channel image are reported in Tables 2, 3 and 4 for maser spots stronger than 10 mJy. The positions of these spots are plotted in Fig. 2. The nearly linear arrangement of the maser spots on the sky is striking. The red- and blue-shifted high-velocity spots straddle the systemic emission complex. This spatial-velocity arrangement is characteristic of a nearly edge-on disk, as is well documented for NGC 4258 (Hermstein et al. 2005).

We calculated the position along the spot distribution (i.e. an impact parameter along position angle of 41° east of north) and show a position-velocity plot in Fig. 3. The high-

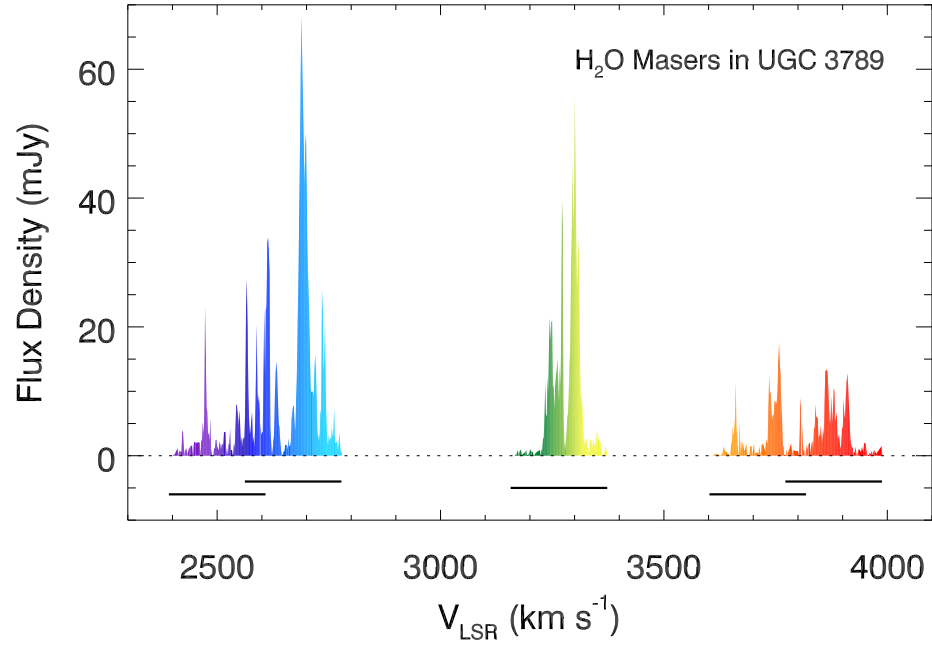


Fig. 1. Interferometer spectrum of the 22 GHz H<sub>2</sub>O masers toward UGC 3789 constructed from VLBI data using the VLBA, the GBT and the Effelsberg antennas. The systemic velocity of the galaxy of  $3325 \pm 24$  km s<sup>-1</sup>, as determined from HI observations, is within the systemic velocity components shown in green colors. High velocity components, shifted by up to 800 km s<sup>-1</sup> from the systemic velocity, are shown in blue and red colors. Broad-band spectra taken with the GBT before the VLBI observations showed almost no detectable maser features outside our observing bands, indicated by horizontal lines below the spectrum.

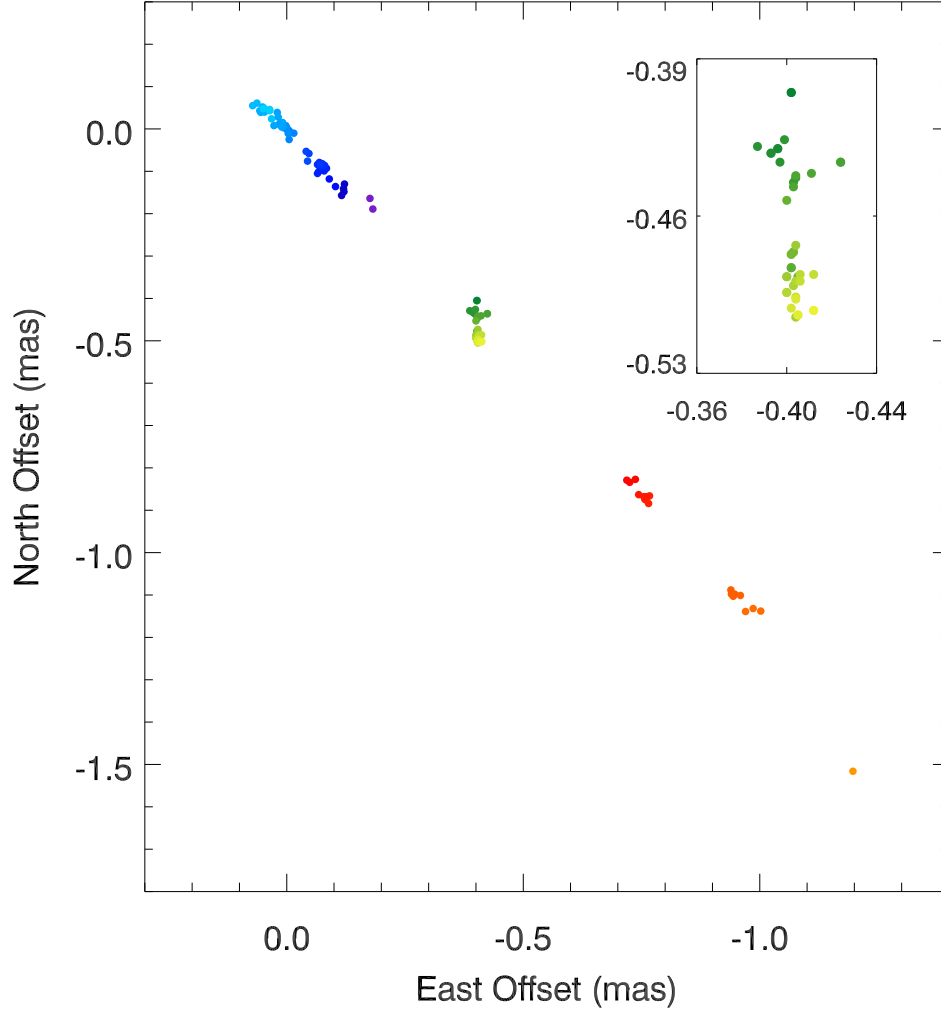


Fig. 2. Map of the relative positions of individual maser spots toward UGC 3789. High velocity blue-shifted (blue) and red-shifted (red) masers straddle the systemic masers (green and expanded view inset) and the linear arrangement of spots suggests that we are viewing a nearly edge-on rotating disk, similar to that seen in NGC 4258. The 2 mas extent of the maser spots in UGC 3789 is approximately seven times smaller than for NGC 4258, which is consistent with UGC 3789 being at approximately seven times greater distance. Formal fitting uncertainties are given in Tables 2, 3 and 4 and are typically  $< 0.010$  mas.

velocity masers display a Keplerian velocity ( $V / \sqrt{1 - \frac{p}{R}}$ ) versus impact parameter (or radius), suggesting that the gravitational potential is dominated by a SMBH. The Keplerian velocity pattern is centered at  $V_{\text{LSR}} = 3265 \text{ km s}^{-1}$ . This is slightly offset from the central velocity of H I emission from the galaxy at  $V_{\text{H I}} = 3325 \pm 24 \text{ km s}^{-1}$  (Theureau et al. 1998). (Note:  $V_{\text{LSR}} - V_{\text{H I}} = 0.3 \text{ km s}^{-1}$  for UGC 3789.) Correcting the maser velocity to the CMB reference frame (i.e.  $V_{\text{CMB}} = V_{\text{LSR}} + 60 \text{ km s}^{-1}$ ), yields a recessional velocity of  $3325 \text{ km s}^{-1}$ . Thus, for  $H_0 = 72 \text{ km s}^{-1} \text{ Mpc}^{-1}$ , UGC 3789's distance would be expected to be  $\sim 46 \text{ Mpc}$ .

The detected blue-shifted high velocity masers sample disk radii between 0.35 and 0.70 mas (0.08 to 0.16 pc) and achieve rotation speeds as high as  $792 \text{ km s}^{-1}$ , with respect to a systemic velocity of  $3265 \text{ km s}^{-1}$ . The detected red-shifted masers sample radii of 0.50 to 1.33 mas (0.11 to 0.30 pc) and achieve rotation speeds up to  $647 \text{ km s}^{-1}$ . Also shown by the straight dotted lines in Fig. 3 is the position-velocity distribution expected for systemic maser spots that lie at a radius of 0.43 mas from the central mass, whose assumed location is indicated by the plus-sign (+) in the figure. These spatial kinematic parameters are comparable to those of the  $\text{H}_2\text{O}$  masers in NGC 4258, which sample radii of 0.14 to 0.28 pc and achieve rotation speeds of  $\sim 1100 \text{ km s}^{-1}$ . The moderately lower rotation speed at a slightly smaller radius suggests that the SMBH at the center of UGC 3789 is less massive than the  $3.9 \times 10^7 M_\odot$  SMBH in NGC 4258. At a distance of 46 Mpc, the high-velocity data for UGC 3789 can be well fit by gas in circular orbit about a central mass of  $1.1 \times 10^7 M_\odot$ , as shown by the blue and red dotted lines in Fig. 3.

As can be seen in Fig. 2, the systemic features lie between the high velocity features but are distributed along a position angle of roughly  $10^\circ$  (east of north). Thus, they are misaligned by approximately  $30^\circ$  with respect to the  $41^\circ$  position angle of the disk, obtained by drawing a line through the high velocity masers. This suggests that the UGC 3789 disk may be slightly inclined and warped and/or that the systemic masers are not all at the same radius. (Note that the NGC 4258 disk is both inclined by  $8^\circ$  with respect to our line of sight and warped (Hernstein et al. 2005).) Deviation from a perfectly flat, edge-on disk for UGC 3789 can also be seen in the position-velocity plot (Fig. 3) as a slight bending of the systemic maser spots and in the variation in accelerations seen by Braatz & Gugliucci (2008). Modeling of the disk will need to accommodate these complications.

We searched for continuum emission from the vicinity of the SMBH (i.e. near the position of the systemic velocity masers) by summing channels 5 through 120 of the (red shifted) dual-circularly polarized band centered at  $V_{\text{LSR}} = 3380 \text{ km s}^{-1}$ . We maximized the detection sensitivity by natural weighting of the data when imaging. The masers were detected at the expected position, offset by  $\sim 1 \text{ mas}$  from the position of the SMBH, but no

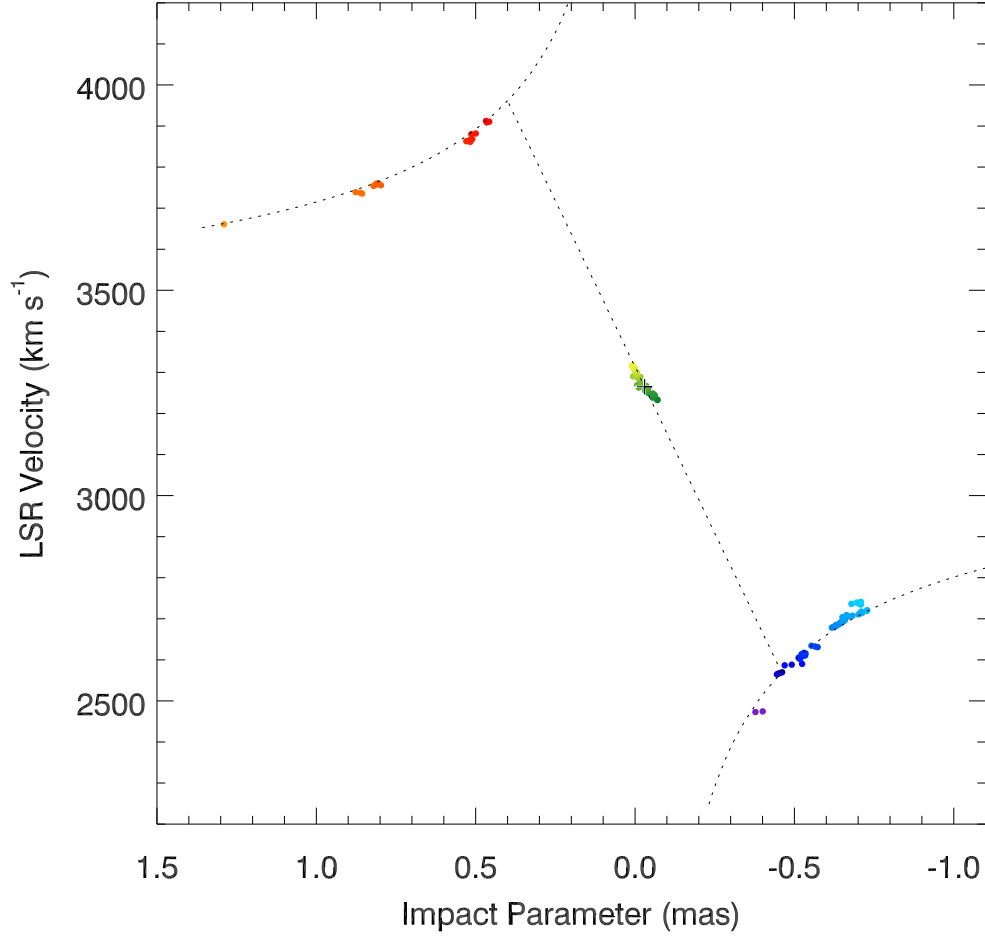


Fig. 3. Position-Velocity plot of the maser spots toward UGC 3789. The high velocity blue-shifted (blue) and red-shifted (red) spots display a Keplerian  $v = R^{-1/2}$  rotation curve, indicated by the curved dotted lines. The systemic masers (green) are consistent with projected positions and velocities for gas in Keplerian orbit at  $R = 0.43$  mas, indicated by the straight dotted line, but small deviations from a linear distribution are apparent. Impact parameter is defined as distance along a position angle of  $41^\circ$  east of north from an (east,north) offset of  $(0.4; 0.5)$  mas; the plus sign (+) at  $(0.03 \text{ mas}, 3265 \text{ km s}^{-1})$  indicates the assumed center of the SMBH.

continuum emission was detected at a 2  $\sigma$  limit of  $< 0.14$  mJy.

#### 4. Conclusions

The discovery of  $\text{H}_2\text{O}$  masers emanating from a sub-pc disk in the Seyfert 2 galaxy NGC 4258 more than two decades ago has led to detailed imaging of an AGN accretion disk. Geometric modeling of the Keplerian orbits of the masers yielded the most accurate distance to any galaxy, allowing recalibration of the extragalactic distance scale. Now, the recent discovery by Braatz & Gugliucci (2008) of  $\text{H}_2\text{O}$  masers in UGC 3789 offers the opportunity to extend this technique to a galaxy seven times more distant.

In this paper we presented VLBI images of the UGC 3789  $\text{H}_2\text{O}$  masers, which showed that these masers are remarkably similar to those in NGC 4258. In both sources, the spatial distribution is nearly linear, with high velocity masers on both sides (both spatially and spectrally) of systemic velocity masers. The masers trace gas in Keplerian orbits with rotation speeds of  $\sim 1000$  km s $^{-1}$  at radii of  $\sim 0.1$  pc, presumably moving under the influence of a  $10^7$  M  $\text{SMBH}$ .

UGC 3789 has a recessional velocity of  $3325$  km s $^{-1}$  and is well into the Hubble flow. The VLBI results presented in this paper will be followed by detailed spectral monitoring data and disk modeling in Paper II to determine the distance to UGC 3789. This angular-diameter distance, when combined with its recessional velocity, should yield a direct and accurate estimate of  $H_0$ .

Facilities: VLBA, GBT, Ebersberg

#### REFERENCES

- Argon, A.L., Greenhill, L.J., Reid, M.J., Moran, J.M. & Humphreys, E.M.L. 2007, *ApJ*, 659, 1040
- Braatz, J.A., Wilson, A.S. & Henkel, C. 1996, *ApJS*, 106, 51
- Braatz, J.A., Henkel, C., Greenhill, L., Moran, J. & Wilson, A. 2004, *ApJ*, 617, L29
- Braatz, J.A. & Gugliucci, N. 2008, *ApJ*, 678, 96
- Braatz et al. 2008 (Paper II), in preparation

- Claussen, M .J. & Lo, K .Y .1986, *ApJ*, 308, 592
- Freedman, W . et al. 2001, *ApJ*, 553, 47
- Greenhill, L .J., Jiang, D .R ., Moran, J.M ., Reid, M .J., Lo, K .Y . & Claussen, M .J.1995a, *ApJ*, 440, 619
- Greenhill, L .J., Henkel, C ., Becker, R ., Wilson, T .L. & Woottenbot, J.G .A .1995b, *A & A* , 304, 21
- Greenhill et al. 2002, *ApJ*, 565, 836
- Greenhill, L .J., Kondratko, P .T ., Lovell, J.E .J., Kuiper, T .B .H ., Moran, J.M ., Jancey, D .L. & Baines, G .P .2003, *ApJ*, 582, L11
- Greenhill, L .J. 2004, *New AR* , 48, 1079
- Haschick, A .D ., Baan, W .A . & Peng, E.W .1994, *ApJ*, 437, L35
- Henkel, C ., Braatz, J.A ., Greenhill, L .J. & Wilson, A .S .2002, *A & A* , 394, L23
- Hernstein et al. 1999, *Nature*, 400, 539
- Hernstein, J.R ., Moran, J.M ., Greenhill, L .J. and Trotter, A .S .2005, *ApJ*, 629, 719
- Hu, W . 2005, *ASP Conf Series Vol 339, Observing Dark Energy*, eds. S.C .W ol & T.R . Lauer (San Francisco: ASP ), 215
- Humphreys, E.M .L ., Reid, M .J., Greenhill, L .J., Moran, J.M . & Argon, A .L .2008, *ApJ*, 672, 800
- Kondratko, P .T . et al. 2006, *ApJ*, 638, 100
- Kondratko, P .T ., Greenhill, L .J. & Moran, J.M . 2006, *ApJ*, 652, 136
- Macri, L.M ., Stanek, K .Z ., Bersier, D ., Greenhill, L .J. & Reid, M .J.2006, *ApJ*, 652, 1133
- Miyoshi, M ., Moran, J., Hernstein, J., Greenhill, L ., Nakai, N ., Diamond, P . & Inoue, M . 1995, *Nature*, 373, 127
- Newman, J.A . et al. 2001, *ApJ*, 553, 562
- Ratra, B . & Peebles, P .J.E .1988, *Phys. Rev. D* , 37, 3406
- Reid, M .J. & Brunthaler, A .2004, *ApJ*, 616, 872

Spergel, D .N .et al. 2003, *ApJS*, 148, 175

Theureau et al. 1998, *A & A S*, 130, 333

Walker, C . & Chatterjee, S., 2000, VLBA Scientific Memo 23,  
<http://www.nrao.edu/memos/sci/gps/ion.html>

Watson, W . & Wallin, B . 1994, *ApJ*, 432, L35

Wetterich, C . 1988, *Nucl. Phys. B*, 302, 668

Table 1. Source Positions

Source	R.A. (J2000) (h m s)	Dec. (J2000) (d ' ")
UGC 3789 .....	07 19 30.9566	59 21 18.330
J0728+ 5907 .....	07 28 47.2170	59 07 34.128
J0753+ 5352 .....	07 53 01.3846	53 52 59.637

Note. | Positions used for data correlation. In aging the UGC 3789 maser spot at  $V_{\text{LSR}} = 2689 \text{ km s}^{-1}$ , by phase-referencing to J0728+ 5907, we found the maser spot offset by ( 1; 15) mas (east,north) from the correlation position.

Table 2. UGC 3789 Red-shifted High-velocity Spots

$V_{\text{LSR}}$ ( $\text{km s}^{-1}$ )	Flux Density ( $\text{m Jy}$ )	$x$ ( $\text{m as}$ )	$x$ ( $\text{m as}$ )	$y$ ( $\text{m as}$ )	$y$ ( $\text{m as}$ )
3912.3.....	11.5	0.737	0.009	0.827	0.013
3910.6.....	13.3	0.719	0.008	0.829	0.012
3908.9.....	12.0	0.725	0.009	0.834	0.013
3881.7.....	10.5	0.744	0.010	0.863	0.015
3880.0.....	11.0	0.760	0.010	0.868	0.014
3868.1.....	10.8	0.755	0.010	0.868	0.014
3866.4.....	13.3	0.757	0.008	0.874	0.012
3864.7.....	14.0	0.760	0.008	0.876	0.011
3863.0.....	13.6	0.765	0.008	0.884	0.011
3861.3.....	13.8	0.767	0.008	0.866	0.011
3761.0.....	13.2	0.940	0.011	1.098	0.015
3759.3.....	15.0	0.944	0.009	1.103	0.014
3757.6.....	18.1	0.947	0.008	1.098	0.011
3755.9.....	14.8	0.939	0.009	1.088	0.014
3754.2.....	10.3	0.959	0.014	1.101	0.020
3738.9.....	10.6	1.002	0.013	1.138	0.019
3737.2.....	10.0	0.986	0.014	1.132	0.020
3735.5.....	13.0	0.970	0.011	1.139	0.016
3660.7.....	12.0	1.197	0.012	1.516	0.017

Note. | Columns 1 and 2 give the LSR velocity and flux density of maser spots in individual spectral channels. Columns 3 (5) and 4 (6) give the east (north) offsets and their uncertainties. Offsets are with respect to the phase reference obtained by summing the emission between velocities 2685 and 2692  $\text{km s}^{-1}$ .

Table 3. UGC 3789 Systemic Velocity Spots

$V_{\text{LSR}}$ ( $\text{km s}^{-1}$ )	Flux Density ( $\text{mJy}$ )	$x$ ( $\text{mas}$ )	$x$ ( $\text{mas}$ )	$y$ ( $\text{mas}$ )	$y$ ( $\text{mas}$ )
3316.0.....	10.1	0.412	0.010	0.502	0.015
3312.6.....	13.7	0.405	0.008	0.504	0.011
3310.9.....	24.1	0.413	0.004	0.488	0.006
3309.2.....	34.2	0.404	0.003	0.497	0.004
3307.5.....	31.6	0.409	0.003	0.498	0.005
3305.8.....	25.9	0.402	0.004	0.501	0.006
3304.1.....	31.1	0.404	0.003	0.496	0.005
3302.4.....	42.3	0.412	0.002	0.486	0.004
3300.7.....	56.4	0.406	0.002	0.489	0.003
3299.0.....	41.8	0.406	0.003	0.486	0.004
3297.3.....	35.7	0.404	0.003	0.489	0.004
3295.6.....	45.9	0.400	0.002	0.494	0.003
3293.9.....	36.4	0.402	0.003	0.483	0.004
3292.2.....	29.4	0.403	0.004	0.491	0.005
3290.5.....	17.7	0.404	0.006	0.505	0.009
3288.8.....	14.9	0.404	0.007	0.473	0.010
3287.1.....	10.8	0.400	0.010	0.487	0.014
3273.5.....	36.2	0.403	0.003	0.476	0.004
3271.8.....	40.1	0.402	0.003	0.477	0.004
3270.1.....	18.5	0.398	0.006	0.477	0.008
3268.4.....	11.2	0.405	0.009	0.487	0.014
3266.7.....	14.4	0.400	0.007	0.453	0.011
3263.3.....	12.2	0.402	0.009	0.483	0.013
3261.6.....	15.5	0.403	0.007	0.447	0.010
3259.9.....	13.9	0.404	0.008	0.442	0.011
3258.2.....	12.8	0.411	0.008	0.441	0.012
3256.5.....	11.3	0.424	0.009	0.436	0.014
3253.1.....	11.6	0.404	0.009	0.443	0.013
3251.4.....	10.9	0.403	0.010	0.447	0.014
3249.7.....	21.4	0.403	0.005	0.445	0.007
3248.0.....	21.3	0.399	0.005	0.426	0.007
3246.3.....	18.3	0.397	0.006	0.436	0.008
3244.6.....	21.9	0.387	0.005	0.429	0.007
3242.9.....	18.6	0.393	0.006	0.432	0.008
3239.5.....	12.8	0.396	0.008	0.430	0.012
3234.4.....	11.8	0.402	0.009	0.405	0.013

Table 4. UGC 3789 Blue-shifted High-velocity Spots

$V_{\text{LSR}}$ ( $\text{km s}^{-1}$ )	Flux Density ( $\text{mJy}$ )	$x$ ( $\text{mas}$ )	$x$ ( $\text{mas}$ )	$y$ ( $\text{mas}$ )	$y$ ( $\text{mas}$ )
2741.4.....	21.5	0.050	0.005	0.048	0.007
2739.7.....	15.2	0.036	0.007	0.043	0.010
2738.0.....	13.8	0.036	0.008	0.046	0.011
2736.3.....	22.8	0.032	0.005	0.024	0.007
2734.6.....	26.6	0.048	0.004	0.049	0.006
2721.0.....	14.2	0.072	0.007	0.055	0.011
2719.3.....	16.2	0.063	0.006	0.061	0.009
2717.6.....	13.4	0.057	0.008	0.043	0.011
2714.2.....	10.5	0.051	0.010	0.052	0.015
2712.5.....	10.4	0.055	0.010	0.039	0.015
2710.8.....	10.4	0.047	0.010	0.040	0.015
2709.1.....	11.2	0.027	0.009	0.008	0.014
2707.4.....	16.9	0.020	0.006	0.039	0.009
2705.7.....	24.1	0.018	0.004	0.028	0.006
2704.0.....	27.3	0.011	0.004	0.005	0.006
2702.3.....	31.1	0.009	0.003	0.014	0.005
2700.6.....	40.7	0.014	0.003	0.012	0.004
2698.9.....	50.7	0.016	0.002	0.011	0.003
2697.2.....	48.7	0.014	0.002	0.011	0.003
2695.5.....	42.7	0.009	0.002	0.015	0.004
2693.8.....	48.5	0.008	0.002	0.006	0.003
2692.1.....	55.8	0.002	0.002	0.008	0.003
2690.4.....	61.3	0.007	0.002	0.003	0.003
2688.7.....	68.8	0.000	0.002	0.003	0.002
2687.0.....	60.4	0.001	0.002	0.000	0.003
2685.3.....	48.4	0.003	0.002	0.010	0.003
2683.6.....	37.5	0.005	0.003	0.004	0.004
2681.9.....	27.5	0.004	0.004	0.011	0.006
2680.2.....	21.8	0.015	0.005	0.010	0.007
2678.5.....	13.3	0.005	0.008	0.025	0.012
2634.3.....	13.5	0.044	0.008	0.076	0.011
2632.6.....	15.1	0.047	0.007	0.058	0.010
2630.9.....	13.4	0.041	0.008	0.053	0.011

Table 4 | Continued

$V_{\text{LSR}}$ ( $\text{km s}^{-1}$ )	Flux Density ( $\text{mJy}$ )	$x$ ( $\text{mas}$ )	$x$ ( $\text{mas}$ )	$y$ ( $\text{mas}$ )	$y$ ( $\text{mas}$ )
2617.3.....	29.0	0.071	0.004	0.084	0.005
2615.6.....	32.3	0.069	0.003	0.079	0.005
2613.9.....	34.4	0.080	0.003	0.086	0.004
2612.2.....	33.6	0.075	0.003	0.082	0.005
2610.5.....	23.9	0.065	0.004	0.084	0.006
2608.8.....	23.0	0.074	0.005	0.088	0.007
2607.1.....	12.6	0.068	0.008	0.100	0.012
2605.4.....	23.5	0.079	0.004	0.099	0.007
2603.7.....	13.0	0.080	0.008	0.112	0.012
2602.0.....	13.6	0.065	0.010	0.105	0.015
2590.1.....	10.4	0.074	0.013	0.089	0.020
2588.4.....	20.9	0.090	0.007	0.118	0.010
2586.7.....	12.8	0.103	0.011	0.136	0.016
2569.7.....	10.7	0.122	0.013	0.130	0.019
2568.0.....	20.2	0.120	0.007	0.141	0.010
2566.3.....	28.0	0.121	0.005	0.148	0.007
2564.6.....	23.7	0.116	0.006	0.157	0.009
2474.5.....	15.7	0.176	0.009	0.164	0.013
2472.8.....	23.7	0.182	0.006	0.189	0.009

Note. | See Table 2